

Approximate Sequential Importance Sampling for Fast Particle Filtering

Ömer Demirel, Ihor Smal, Wiro J. Niessen, Erik Meijering and Ivo F. Sbalzarini

Abstract—Particle filters are key algorithms for object tracking under non-linear, non-Gaussian dynamics. The high computational cost of particle filters, however, hampers their applicability in cases where the likelihood model is costly to evaluate, or where large numbers of particles are required to represent the posterior. We introduce the approximate sequential importance sampling/resampling (ASIR) algorithm, which aims at reducing the cost of traditional particle filters by approximating the likelihood with a mixture of uniform distributions over pre-defined cells or bins. The particles in each bin are represented by a dummy particle at the center of mass of the original particle distribution and with a state vector that is the average of the states of all particles in the same bin. The likelihood is only evaluated for the dummy particles, and the resulting weight is identically assigned to all particles in the bin. We derive upper bounds on the approximation error of the so-obtained piecewise constant function representation, and analyze how bin size affects tracking accuracy and runtime. Further, we show numerically that the ASIR approximation error converges to that of sequential importance sampling/resampling (SIR) as the bin size is decreased. We present a set of numerical experiments from the field of biological image processing and tracking that demonstrate ASIR’s capabilities. Overall, we consider ASIR a promising candidate for simple, fast particle filtering in generic applications.

Index Terms—Particle filters, sequential Bayesian estimation, sequential importance sampling.

I. INTRODUCTION

SINCE their inception, sequential Monte Carlo (SMC) resampling methods (a.k.a., particle filters) [1]–[3] have emerged as a useful tool to estimate and track targets with non-linear and/or non-Gaussian dynamics. Unlike the Kalman filter [4], [5] and its variants [6], particle filters (PF) do not use a fixed functional form of the posterior probability density function (PDF). Instead, they employ a finite number of points, called “particles”, to discretely approximate the posterior probability density function (PDF) in state space [7].

A standard PF algorithm consists of two parts: (i) sequential importance sampling (SIS) and (ii) resampling [2]. A popular combined implementation of these two parts is the sequential importance resampling (SIR) algorithm. Depending on the application, SIR may need a large number of particles to adequately sample the state space. This demands substantial

computational resources that scale linearly with the number of particles.

Here, we introduce the *approximate SIR* (ASIR) algorithm, which reduces the computational cost of SIR while providing tracking accuracy comparable to standard SIR. The main idea behind ASIR is to group particles in state space (i.e., creating *bins*) and to represent each group of particles by a single *representative particle*. Only the weight of this representative dummy particle is then updated. We choose the dummy particle to sit in the center of mass of the group of particles it represents and to carry the mean properties of all the particles in the respective group. Once the weight of the dummy particle is computed, all other particles in the same group receive the same weight, which is copied from the dummy instead of being re-computed through the likelihood model for each individual particle, as in the original SIR. This way, an ASIR-based PF can outperform a classical SIR-based PF by orders of magnitude in applications where evaluation of the likelihood is computationally expensive.

We outline the mathematical roots of ASIR and derive an upper bound on the expected approximation error with respect to the chosen *bin* (i.e., Cartesian mesh *cell* in 2D) size. This error stems from the point-wise approximation of the likelihood function and is quantified using mid-point Riemann-sum error analysis [8], [9]. We numerically quantify the errors in the state estimates (based on the posterior distribution) obtained by SIR and ASIR as a function of the number of particles used, and show that there is almost no difference between SIR and ASIR in terms of tracking accuracy. Furthermore, with a focus on biological image processing, we show that relating the bin size to the pixel size of an image provides satisfactory, and sometimes even higher-quality results in ASIR compared with standard SIR.

The structure of this manuscript is as follows: Section II summarizes recent related advancements in the PF field. Section III recapitulates the classical SIR algorithm, whereas Section IV introduces our new ASIR method, discusses the theoretical framework behind ASIR, and provides detailed pseudocode. In Section V, we benchmark ASIR against SIR in terms of tracking accuracy, runtime, and error convergence using two different likelihood functions and different types of images. Finally, Section VI discusses the results and concludes the manuscript with an outlook.

II. RELATED WORKS

Bayesian approaches based on *belief propagation* are often used to solve *global localization problems* [10], [11]. There,

Ö. Demirel and I.F. Sbalzarini are with the MOSAIC Group, Center of Systems Biology Dresden (CSBD), Max Planck Institute of Molecular Cell Biology and Genetics, Pfotenhauerstr. 108, 01307 Dresden, Germany. email: {demirel,ivos}@mpi-cbg.de

I. Smal, E. Meijering, and W. Niessen are with the Biomedical Imaging Group Rotterdam, Departments of Medical Informatics and Radiology, Erasmus MC – University Medical Center Rotterdam, Rotterdam, The Netherlands.

an agent tries to estimate its position in the absence of prior knowledge. To address this problem, many different localization algorithms have been proposed. In *Markov localization* (ML) [11], [12], the initial belief is a uniformly random distribution. The belief is then propagated in a Bayesian framework by including *perception* data. For the posterior belief, usually a histogram filter [7] is used whose grid cell size and thus the grid resolution depends on the desired accuracy. The second approach contains a popular group of algorithms called Monte Carlo localization (MCL) algorithms [13], [14] that are by design similar to PF. Here, the belief is propagated by a set of weighted samples (i.e., particles) that recursively undergo SIR. The main difference between MCL and PF is the number of particles used, which changes according to the *mode* of the problem. In the *exploration* or *discovery* mode, the sample size is increased in order to globally locate the agent. Once localization is done, the *tracking* mode uses fewer particles to track the agent's movement. The original MCL algorithm suffers from the *kidnapping* problem (re-localization after disappearance of the agent due to a random jump) [13], [15]. To overcome this, several MCL extensions (e.g., SRL [16], Mix-MCL [17], A-MCL [17], and KLD-Sampling [18]) have been proposed. Later, several hybrid methods (e.g., R-MCL [19] and Moving Grid Cell Based MCL [20]) were also introduced. These hybrid algorithms switch between ML and MCL depending on the mode of the problem. Moving Grid Cell Based MCL [20] was further improved by dynamically changing the size of the grid cells [21].

The box particle filter (BPF) [22] is based on interval analysis [23]. It uses box-shaped particles as an alternative to point particles. BPF is especially useful in situations where the posterior is wide [24], which can be successfully captured by box particles. Despite its advantages, however, BPF is not well understood and lacks important theoretical background, such as a proof of convergence and insight into the resampling step [25]. Also, its exact computational cost yet needs to be investigated and compared with traditional PF.

III. THE CLASSICAL SIR PARTICLE FILTER

Recursive Bayesian importance sampling [26] of an unobserved and discrete Markov process $\{\mathbf{x}_k\}_{k=1,\dots,K}$ is based on three components: (i) the measurement vector $\mathbf{Z}^k = \{\mathbf{z}_1, \dots, \mathbf{z}_k\}$, (ii) the dynamics (i.e., state transition) probability distribution $p(\mathbf{x}_k|\mathbf{x}_{k-1})$, and (iii) the likelihood $p(\mathbf{z}_k|\mathbf{x}_k)$. Then, the state posterior $p(\mathbf{x}_k|\mathbf{Z}^k)$ at time k is recursively computed as:

$$\underbrace{p(\mathbf{x}_k|\mathbf{Z}^k)}_{\text{posterior}} = \frac{\overbrace{p(\mathbf{z}_k|\mathbf{x}_k)}^{\text{likelihood}} \overbrace{p(\mathbf{x}_k|\mathbf{Z}^{k-1})}^{\text{prior}}}{\underbrace{p(\mathbf{z}_k|\mathbf{Z}^{k-1})}_{\text{normalization}}}, \quad (1)$$

where the prior is defined as:

$$p(\mathbf{x}_k|\mathbf{Z}^{k-1}) = \int p(\mathbf{x}_k|\mathbf{x}_{k-1}) p(\mathbf{x}_{k-1}|\mathbf{Z}^{k-1}) d\mathbf{x}_{k-1}. \quad (2)$$

In the PF approach, the posterior at each time point k is approximated by N weighted samples (i.e., particles)

$\{\mathbf{x}_k^i, w_k^i\}_{i=1,\dots,N}$. This approximation is achieved by drawing a set of particles from an importance function (i.e., proposal distribution) $\pi(\cdot)$ and updating their weights according to the dynamics PDF and the likelihood. This process is called sequential importance sampling (SIS) [2]. However, SIS suffers from the *weight degeneracy*, where small particle weights become even smaller and do not contribute to the posterior any more. To overcome this, a *resampling* step is performed [2] whenever the sample size falls below a preset threshold. Using the standard notation, as in Refs. [2], [27], the complete SIR algorithm is given in Algorithm 1.

Algorithm 1 Sequential Importance Resampling (SIR)

```

1: procedure SIR
2:   for  $i = 1 \rightarrow N$  do                                ▷ Initialization,  $k=0$ 
3:      $w_0^i \leftarrow 1/N$ 
4:     Draw  $\mathbf{x}_0^i$  from  $\pi(\mathbf{x}_0)$ 
5:   end for
6:   for  $k = 1 \rightarrow K$  do
7:     for  $i = 1 \rightarrow N$  do                                ▷ SIS step
8:       Draw a sample  $\tilde{\mathbf{x}}_k^i$  from  $\pi(\mathbf{x}_k|\mathbf{x}_{k-1}^i, \mathbf{Z}^k)$ 
9:       Update the importance weights
10:       $\tilde{w}_k^i \leftarrow w_{k-1}^i \frac{p(\mathbf{z}_k|\tilde{\mathbf{x}}_k^i)p(\tilde{\mathbf{x}}_k^i|\mathbf{x}_{k-1}^i)}{\pi(\tilde{\mathbf{x}}_k^i|\mathbf{x}_{k-1}^i, \mathbf{Z}^k)}$ 
11:    end for
12:    for  $i = 1 \rightarrow N$  do
13:       $w_k^i \leftarrow \tilde{w}_k^i / \sum_{j=1}^N \tilde{w}_k^j$ 
14:    end for
15:     $\hat{N}_{\text{eff}} \leftarrow 1 / \sum_{j=1}^N (w_k^j)^2$                                 ▷ Calculate the effective sample size
16:    if  $\hat{N}_{\text{eff}} < N_{\text{threshold}}$  then                                ▷ Resampling step
17:      Sample a set of indices  $\{s(i)\}_{i=1,\dots,N}$  distributed such that  $\Pr[s(i) = l] = w_k^l$  for  $l = 1 \rightarrow N$ .
18:      for  $i = 1 \rightarrow N$  do
19:         $\mathbf{x}_k^i \leftarrow \tilde{\mathbf{x}}_k^{s(i)}$ 
20:         $w_k^i \leftarrow 1/N$                                 ▷ Reset the weights
21:      end for
22:    end if
23:  end for
24: end procedure

```

IV. THE APPROXIMATE SIR PARTICLE FILTER

In classical SIR, all particle weights are updated according to the likelihood, which may impart a high computational load. Moreover, the computational cost scales linearly with the number of particles. Therefore, depending on the application, the likelihood evaluation often constitutes the most time-consuming part of a PF.

To address this problem, we propose the ASIR algorithm, which aims at reducing the computational cost of importance weight update. We do this by grouping the particles into non-overlapping *bins* (i.e., Cartesian mesh cells), which are then represented by only a single dummy particle positioned at the center of mass of the real particles in that bin. The center of mass is computed using the state vectors and weights of all particles within the bin and is solely used to *represent* that bin by a single *dummy particle*.

The importance weight update is then only applied to the dummy particle. All other particles in the same bin are assigned the same weight that the dummy particle received. Thus, we approximate the likelihood by a mixture of uniform PDFs and bypass the costly likelihood update step for all particles. The ASIR algorithm differs from SIR only in the SIS part, where the particles are binned and several averaging operations are performed. The detailed pseudo-code is given in Algorithm 2.

Algorithm 2 Approximate Sequential Importance Sampling/Resampling (ASIR)

```

1: procedure ASIR
2:   for  $i = 1 \rightarrow N$  do                                 $\triangleright$  Initialization,  $k=0$ 
3:      $w_0^i \leftarrow 1/N$ 
4:     Draw  $\mathbf{x}_0^i$  from  $\pi(\mathbf{x}_0)$ 
5:   end for
6:   Create  $B$  bins of equal size  $I_{1,\dots,B}$ 
7:   for  $k = 1 \rightarrow K$  do
8:     for  $i = 1 \rightarrow N$  do                                 $\triangleright$  ASIS step
9:       Draw a sample  $\tilde{\mathbf{x}}_k^i$  from  $\pi(\mathbf{x}_k|\mathbf{x}_{k-1}^i, \mathbf{Z}^k)$ 
10:      Assign  $\tilde{\mathbf{x}}_k^i$  to a bin
11:    end for
12:    for  $j = 1 \rightarrow B$  do                                 $\triangleright$  Visit all bins
13:       $\triangleright$  Create a representative particle that has the mean
        values of the state vector of all particles in the same bin
14:       $\mathbf{x}_{\text{dum}} \leftarrow \text{mean}\{\tilde{\mathbf{x}}_k^1, \dots, \tilde{\mathbf{x}}_k^{N_{I_j}}\}$ 
15:      Update the importance weights
16:       $w_{\text{dum}_k} \leftarrow w_{\text{dum}_{k-1}} \frac{p(\mathbf{z}_k|\mathbf{x}_{\text{dum}})p(\mathbf{x}_{\text{dum}}|\mathbf{x}_{k-1}^i)}{\pi(\mathbf{x}_{\text{dum}}|\mathbf{x}_{k-1}^i, \mathbf{Z}^k)}$ 
17:      for all  $\tilde{\mathbf{x}}_k^i$  in bin  $I_j$  do
18:         $w_k^i \leftarrow w_{\text{dum}_k}$ 
19:      end for
20:    end for
21:     $\triangleright$  Calculate the effective sample size
     $\hat{N}_{\text{eff}} \leftarrow 1 / \sum_{j=1}^N (w_k^j)^2$ 
22:    if  $\hat{N}_{\text{eff}} < N_{\text{threshold}}$  then                     $\triangleright$  Resampling step
23:      Sample a set of indices  $\{s(i)\}_{i=1,\dots,N}$  distributed
        such that  $\Pr[s(i) = l] = w_k^l$  for  $l = 1 \rightarrow N$ .
24:      for  $i = 1 \rightarrow N$  do
25:         $\mathbf{x}_k^i \leftarrow \mathbf{x}_k^{s(i)}$ 
26:         $w_k^i \leftarrow 1/N$                              $\triangleright$  Reset the weights
27:      end for
28:    end if
29:  end for
30: end procedure

```

The idea behind ASIR is conceptually related to using *box particles*, where the box support is approximated by a mixture of piecewise constant functions [28]. Gning *et al.* [25], [28] use sophisticated interval analysis [23] to show that the uniform PDF approximation of the posterior becomes more accurate as the number of *intervals* increases. It is, however, unclear how many intervals one has to use and what value the uniform PDF in an interval should have.

With ASIR, we provide a simple way of using uniform PDFs to approximate the likelihood function, which eventually results in a satisfactory posterior representation through the

Bayesian formulation. Moreover, it requires only few modifications to the classical SIR, which makes ASIR an attractive choice for practical implementations.

A. Theoretical framework

The ASIR algorithm is a function-approximation algorithm. It divides the n -dimensional state space in n -dimensional bins. In each bin, a sufficiently differentiable likelihood function is approximated by a constant value. The error analysis of such piecewise constant approximations is well understood on the basis of Taylor's theorem for multivariate functions.

For the sake of practicality in real-world applications, we present the theoretical framework of ASIR with a focus on image processing. When processing a sequence of 2D images, the likelihood function $p(\mathbf{z}_k|\mathbf{x}_k)$ is typically a two-dimensional function that is discretized over a finite set of particles. In SIR, the likelihood is approximated by N particles, where the particle number N defines the accuracy for the specific application. Therefore, the approximation error of SIR is denoted $\mathcal{E}_{\text{SIR}}(N)$.

With ASIR, only the positions of the particles play a role in the likelihood update. This allows ASIR to bin the state space. Therefore, the approximation error in $p(\mathbf{z}_k|\mathbf{x}_k)$ depends on both on the number of particles N and the maximum lengths of the bins l_x and l_y in both dimensions. Hence, the overall approximation error of ASIR is denoted $\mathcal{E}_{\text{ASIR}}(N, l_x, l_y)$.

First, we analyze the effect of bin size on $\mathcal{E}_{\text{ASIR}}(N, l_x, l_y)$. For that purpose, we consider two cases: The first considers bins of varying rectangular shapes (i.e., $l_x \neq l_y$). In this setting, we fix N and let the approximation error depend on the bin lengths in both dimensions, hence $\mathcal{E}_{\text{ASIR}}(l_x, l_y)$. In the second case, all cells are squares of edge length l . The ASIR approximation error can then be expressed as $\mathcal{E}_{\text{ASIR}}(l)$.

Second, we compare SIR with an ASIR in which each bin corresponds to a single pixel in a “pseudo”-tracking test case (see Section V). In this comparison, we assume Gaussian and uniform priors of different sizes. A smooth likelihood function is approximated by SIR and ASIR and later applied to the prior. Thus, we obtain the estimation errors for the state. We call this experiment “pseudo”-tracking, since by eliminating the explicit dynamics PDF, we can focus on the approximation error and its convergence with increasing N .

B. The effect of cell size on $\mathcal{E}_{\text{ASIR}}$

The particle locations in a cell cannot be determined *a priori* since the movement of the particles depends on the data. We assume that for small cells and statistically large numbers of particles, we have a uniform particle distribution within a cell. For this case we analyze the approximation error introduced by the ASIR algorithm.

Approximating integrable functions by piecewise constant functions is well understood in mathematics on the basis of Riemann integral theory [8], [9]. We formulate the approximation error $\mathcal{E}_{\text{ASIR}}(l_x, l_y)$ of ASIR with rectangular cells (Theorem 1), and then simplify it to $\mathcal{E}_{\text{ASIR}}(l)$ for square cells in Theorem 2. All results can be extended to higher-dimensional settings.

Theorem 1. Let the likelihood $p(\mathbf{z}_k|\mathbf{x}_k)$ be a twice continuously differentiable function $f(x, y)$ within a domain $D \in \mathbb{R}^{[x_0, x_n] \times [y_0, y_m]}$, which is divided into $B = n \times m$ non-overlapping rectangular cells. Further, l_{k_i} and l_{k_j} denote the width (i.e., in x -direction) and the height (i.e., in y -direction) of cell I_k in D , where $D = \bigcup_{k=1}^B I_k$. The indices i and j are given by $i = 1, \dots, n$ and $j = 1, \dots, m$, and the maximum side lengths in both dimensions are defined as $l_x = \max_{k_i}(l_{k_i})$ and $l_y = \max_{k_j}(l_{k_j})$ where $l_{k_i} = x_k - x_{k-1}$ and $l_{k_j} = y_k - y_{k-1}$. Then, the total approximation error $\mathcal{E}_{ASIR}(l_x, l_y)$ of the likelihood in D obtained by ASIR (Algorithm 2) is bounded by:

$$\mathcal{E}_{ASIR}(l_x, l_y) \leq \frac{1}{24} \left[\max_{[D]} |f_{xx}| l_x^3 l_y + \max_{[D]} |f_{yy}| l_x l_y^3 \right],$$

where $\max_{[x_0, x_n]} |f_{xx}|$ and $\max_{[y_0, y_m]} |f_{yy}|$ are the maxima of the absolute values of $\frac{\partial^2 f}{\partial x^2}$ and $\frac{\partial^2 f}{\partial y^2}$ in D , respectively.

Considering only equi-sized square cells, Theorem 1 simplifies to:

Theorem 2. Let the likelihood $p(\mathbf{z}_k|\mathbf{x}_k)$ be a twice continuously differentiable function $f(x, y)$ within a square domain $D \in \mathbb{R}^{[x_0, x_m] \times [y_0, y_m]}$, which is divided into $B = m^2$ non-overlapping square cells. Further, $D = \bigcup_{k=1}^B I_k$ where region I_k has width and height $|x_i - x_{i-1}| = |y_j - y_{j-1}| = l$ with $i = j = \{1, \dots, m\}$. Then, the total approximation error $\mathcal{E}_{ASIR}(l)$ of the likelihood in D obtained by ASIR (Algorithm 2) is bounded by:

$$\mathcal{E}_{ASIR}(l) \leq \frac{l^4}{24} \left[\max_{[D]} |f_{xx}| + \max_{[D]} |f_{yy}| \right].$$

Appendix A provides a proof of Theorem 1, and Appendix B includes the explanation of Theorem 2.

In ASIR, the state space is decomposed into non-overlapping cells. Choosing an appropriate cell size is hence crucial for ASIR. Similar to histogram filters [7], the accuracy of ASIR is determined by the cell size. In the highest possible resolution, there is one particle per cell, which recovers the classical SIR algorithm.

In image processing, it is convenient to choose the image pixels as the cells of ASIR. This constitutes a good choice since in typical image-processing applications, the pixel size already reflects the sizes of the objects represented in the image in order not to under-sample the objects and not to store unnecessary data. We call ASIR with single-pixel cells ASIR-1x1. Due to the characteristics of the likelihood function, however, there may be cases where sub-pixel resolution or higher accuracy is needed. Therefore, we also investigate ASIR-2x2, where each pixel is divided into four cells. In the following Section, we empirically benchmark the effect of cell size on ASIR performance and accuracy.

V. EXPERIMENTAL RESULTS

We study the performance of the proposed ASIR by considering a biological image-processing application: the tracking of sub-cellular (here, “cell” refers to the biological cell being imaged and is not to be confused with the ASIR bin

cells) objects imaged by fluorescence microscopy [29]–[31]. There, intracellular structures such as endosomes, vesicles, mitochondria, or viruses are labeled with fluorescent proteins and imaged over time with a confocal microscope. Many biological studies start from analyzing the dynamics of those structures and extracting parameters that characterize their behavior, such as average velocity, instantaneous velocity, spatial distribution [32], motion correlations, etc.

A. Dynamics model

The motion of sub-cellular objects can be represented by a variety of dynamics models, ranging from random walks to constant-velocity models to more complex dynamics where switching between motion types occurs [33], [34].

Here, we use a nearly-constant-velocity model, which is frequently used in practice [35]. The state vector in this case is $\mathbf{x} = (\hat{x}, \hat{y}, v_x, v_y, I_0)^T$, where \hat{x} and \hat{y} are the x - and y -positions of an object, (v_x, v_y) its velocity vector, and I_0 its fluorescence intensity.

B. Likelihood / Appearance model

Many sub-cellular objects are smaller than what can be resolved by the microscope, making them appear in a fluorescence image as diffraction-limited bright spots with an intensity profile given by the impulse-response function of the microscope, the so-called point-spread-function (PSF) [31]–[33], [35].

In practice, the PSF of a fluorescence microscope is well approximated by a 2D Gaussian [36], [37]. Object appearance in a 2D image is hence modeled as:

$$I(x, y; x_0, y_0) = I_0 \exp \left(-\frac{(x - x_0)^2 + (y - y_0)^2}{2\sigma_{\text{PSF}}^2} \right) + I_{\text{bg}}, \quad (3)$$

where (x_0, y_0) is the position of the object, I_0 is its intensity, I_{bg} is the background intensity, and σ_{PSF} is the standard deviation of the Gaussian PSF. Typical microscopes yield images with pixel edge lengths corresponding to 60 to 200 nm real-world length in the imaged sample. For the images used here, the pixel size is 67 nm and the microscope has $\sigma_{\text{PSF}} = 78$ nm (or 1.16 pixels). During image acquisition, the “ideal” intensity profile $I(x, y)$ is corrupted by measurement noise, which in the case of fluorescence microscopy has mixed Gaussian-Poisson statistics. For the resulting noisy image $\mathbf{z}_k = Z_k(x, y)$ at time point k , the likelihood $p(\mathbf{z}_k|\mathbf{x}_k)$ is:

$$p(\mathbf{z}_k|\mathbf{x}_k) \propto \exp \left(-\frac{1}{2\sigma_\xi^2} \sum_{\xi(x_i, y_i) \in \mathcal{S}_\mathbf{x}} [Z_k(x_i, y_i) - I(x_i, y_i; \hat{x}, \hat{y})]^2 \right), \quad (4)$$

where σ_ξ controls the peakiness of the likelihood, (x_i, y_i) are the integer coordinates of the pixels in the image, (\hat{x}, \hat{y}) are the spatial components of the state vector \mathbf{x}_k , and $\mathcal{S}_\mathbf{x}$ defines a small region in the image centered at the object location specified by the state vector \mathbf{x}_k . Here, $\mathcal{S}_\mathbf{x} = [\hat{x} - 3\sigma_{\text{PSF}}, \hat{x} + 3\sigma_{\text{PSF}}] \times [\hat{y} - 3\sigma_{\text{PSF}}, \hat{y} + 3\sigma_{\text{PSF}}]$.

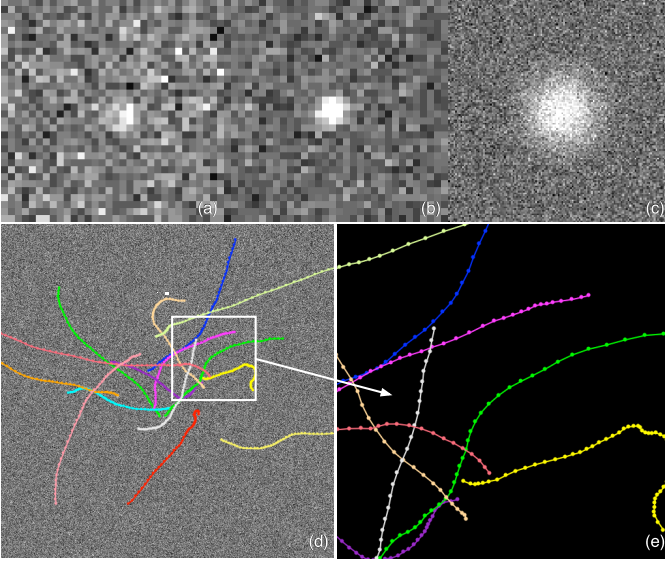


Fig. 1: Examples of object appearance for different object sizes and SNR: (a) $\sigma_{\text{PSF}} = 1.16$, SNR=2, (b) $\sigma_{\text{PSF}} = 1.16$, SNR=4, (c) $\sigma_{\text{PSF}} = 13$, SNR=2. (d/e): Typical object trajectories generated using the nearly-constant-velocity dynamics model.

C. Experimental setup

We focus on single sub-cellular object tracking and compare ASIR with SIR in two test cases, which differ in the size of the tracked object. We consider two different object sizes in order to compare cases where the likelihood is computationally cheap to evaluate with cases where this is more costly. 20 synthetic image sequences of different quality (i.e., signal-to-noise ratios (SNR)) are generated by simulating a microscope. Each sequence is composed of 50 frames of size 512×512 pixels. The movies show a single object moving according to the dynamics model. Examples are shown in Fig. 1.

The two object sizes correspond to $\sigma_{\text{PSF}} = 1.16$ and $\sigma_{\text{PSF}} = 13$, and are named “small object tracking” and “large object tracking”, respectively (Fig. 1(a-c)). The positions and directions of motion of the objects are randomly chosen within the image plane. The speed (i.e., the displacement in pixels per frame) is drawn uniformly at random over the interval $[2, 7]$ for large objects and over $[2, 4]$ for small objects. The SNR of the images of large objects is 2, that for small objects is 4. We use the SNR definition for Poisson noise [38]. In the literature on sub-cellular object tracking, a SNR of 4 is considered critical, as for lower SNRs many of the available tracking methods fail [36].

Knowing the ground-truth object positions and those estimated by the PF, we quantify the tracking accuracy by the root-mean-square error (RMSE) in units of pixels. The likelihood kernel for the large objects has a support of 65×65 pixels and is correspondingly costly to evaluate. The kernel for the small objects has a support of 9×9 pixels and is cheaper to evaluate. Examples of noise-free and noisy object profiles, together with their likelihood kernels, are shown in Fig. 2.

Using double-precision arithmetics, a single PF particle requires 52 KB (i.e., six doubles and one integer) of computer memory. The particles are initialized at the ground-truth loca-

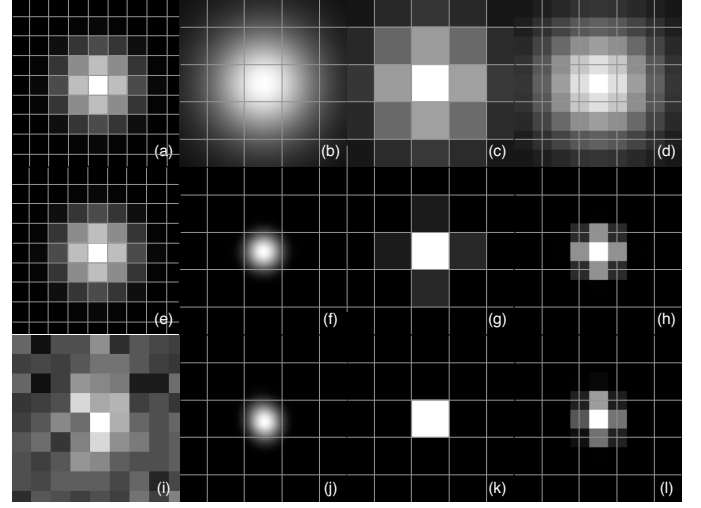


Fig. 2: Examples of likelihood profiles. The noise-free objects are shown in (a, e), and the noisy (SNR=2) object in (i) with $\sigma_{\text{PSF}} = 1.16$. We show the corresponding likelihood kernels (b, f, j), the approximated likelihoods used by ASIR-1x1 (c, g, k), and the approximated likelihoods used by ASIR-2x2 (d, h, l). In (b, c, d) the parameter σ_{ξ} is 30, for the rest $\sigma_{\xi} = 10$. The distance between the grid-lines corresponds to the size of the image pixel.

tion and all tests are repeated 50 times for different realizations of the image-noise process on a single core of a 12-core Intel® Xeon® E5-2640 2.5 GHz CPU with 128 GB DDR3 800 MHz memory on the MPI-CBG’s MadMax computer cluster. All algorithms are implemented in Java (v. 1.7.0_13) within the Parallel Particle Filtering (PPF) library [39]. The results are summarized in Figs. 3 and 4 for large and small objects, respectively.

D. Results

When tracking large objects (Fig. 3), both ASIR versions provide significant speedups over the classical SIR algorithm. For 12 800 particles, ASIR-1x1 is more than two orders of magnitude faster than SIR with a 2.4% loss in tracking accuracy. ASIR-2x2 provides an up to 5.8% better tracking accuracy than SIR while running over 50 times faster. Since SIR is also an approximation of the actual posterior distribution, in some cases ASIR may provide a better representation of the posterior and thus a higher tracking accuracy. This phenomenon has been previously described [40].

When tracking small objects, the likelihood support requires sub-pixel resolution and the effect of bin size is more visible (Fig. 4). ASIR-1x1 uses rather coarse bins compared to the likelihood support (Fig. 2), resulting in a pronounced loss of tracking accuracy. Visually, however, the trajectories produced by SIR and ASIR-1x1 are virtually indistinguishable, since the tracking accuracy of ASIR-1x1 is still in the sub-pixel regime (about 0.27 pixel). When finer bins (ASIR-2x2) are used, the tracking accuracy of ASIR is again better than that of SIR, and ASIR runs more than five times faster than SIR.

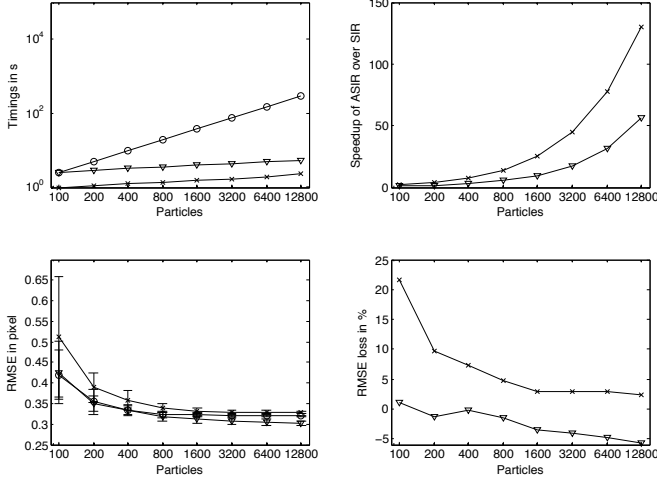


Fig. 3: Runtime performance and tracking accuracy of ASIR-1x1 (\times) and ASIR-2x2 (∇) compared with SIR (\circ) for a 65 pixel wide likelihood kernel. The number of particles used starts from 100 and is doubled for each case until 12 800. The timings of all three methods are presented in log-log scale (upper left), whereas the relative speedups of the ASIR methods over SIR are shown in the upper-right plot. The accuracy loss (lower right) of ASIR-1x1 drops rapidly as the number of particles in the system is increased. Error bars show standard deviations across the 50 repetitions of each experiment.

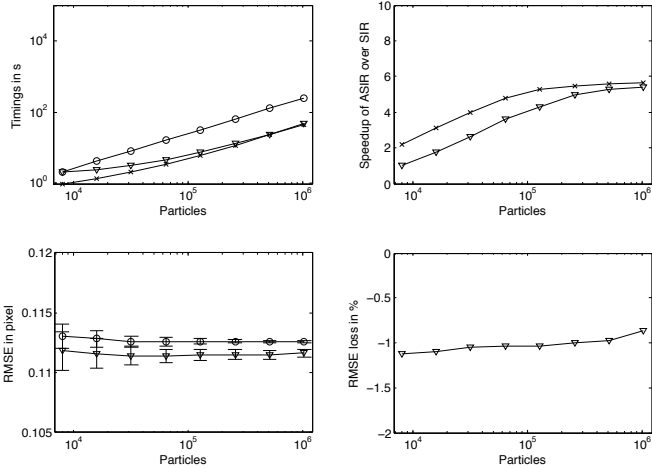


Fig. 4: Runtime performance and tracking accuracy of ASIR-1x1 (\times) and ASIR-2x2 (∇) compared with SIR (\circ) for a nine-pixel wide likelihood kernel. The number of particles used starts from 8 000 and is doubled for each case until 1 024 000. The timings of all three methods are presented in log-log scale (upper left), whereas the relative speedups of the ASIR methods over SIR are shown in the upper-right plot. For the accuracy comparisons (lower left), we show only the results for ASIR-2x2 and SIR, since ASIR-1x1’s coarse bin resolution reduces the computational cost of SIR and enables tackling larger problems as well as tackling mid-size problems in real time. In some configurations, especially when sub-pixel resolution is used for the bins, ASIR may yield more accurate results than SIR. Error bars show standard deviations across the 50 repetitions of each experiment.

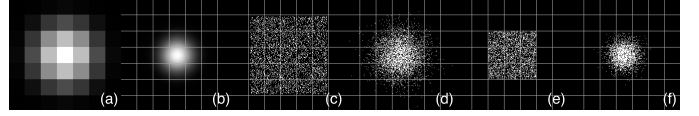


Fig. 5: The “pseudo”-tracking experiment: (a) the object with $\sigma_{\text{PSF}} = 1.16$, $\text{SNR}=2$; (b) the corresponding likelihood with $\sigma_{\xi} = 20$; (c) a uniform prior of support 5×5 pixel; (d) a Gaussian prior with $\sigma_{\text{prior}} = 0.5$; (e) a uniform prior of support 3×3 pixel; (f) a Gaussian prior with $\sigma_{\text{prior}} = 0.8$. Thin white lines indicate the image pixel grid.

E. Convergence of SIR and ASIR

Both SIR and ASIR employ particle approximations of a smooth, differentiable function, the order of accuracy of which depends on the number of particles N . In order to eliminate uncertainties resulting from the dynamics model, we assume the prior $p(\mathbf{x}_t | \mathbf{Z}^{t-1})$ to be either a uniform distribution over 3×3 or 5×5 pixels, or a Gaussian with $\sigma_{\text{prior}} = \{0.5, 0.8\}$, respectively. We then evaluate the likelihood in Eq. (4) with $\sigma_{\xi} = 20$ using both SIR and ASIR. We call this a “pseudo”-tracking experiment. The object is a single PSF (Eq. (3)) with $\sigma_{\text{PSF}} = 1.16$. Visualizations of the object, likelihood, and prior are shown in Fig. 5.

We compare two versions of the ASIR method which differ in the placement of the dummy particles: In ASIR-CoC, the dummy particles are placed at the geometric centers of the bins, whereas in ASIR-CoM, the centers of mass of the state vectors of all particles inside that bin are used. Each convergence experiment is repeated 1000 times for different realizations of the random process, and the number of particles is increased up to 100 000. We quantify the RMSE of the state estimation as a function of the number of particles used. The resulting convergence plots for ASIR and SIR are shown in Fig. 6.

We observe no significant differences between SIR and the two ASIR variants. The error of ASIR-CoM is always slightly lower than that of ASIR-CoC. SIR is generally the most accurate, but is outperformed by ASIR-CoM in some cases, confirming our experimental tests as well as the findings in Ref. [40]. As N increases, the errors of all methods decrease, and the difference in the errors of SIR and ASIR shrink. In all cases, however, the runtimes of both ASIR variants was significantly less than that of SIR.

VI. CONCLUSIONS

We proposed a fast approximate SIR algorithm, called ASIR. ASIR is based on spatially binning particles in *cells* and representing each cell by a single dummy particle at the center of mass of the cell’s particle distribution, carrying the average state vector of all particles in that cell. This approximates the likelihood by a mixture of uniform PDFs. ASIR significantly reduces the computational cost of SIR and enables tackling larger problems as well as tackling mid-size problems in real time. In some configurations, especially when sub-pixel resolution is used for the bins, ASIR may yield more accurate results than SIR.

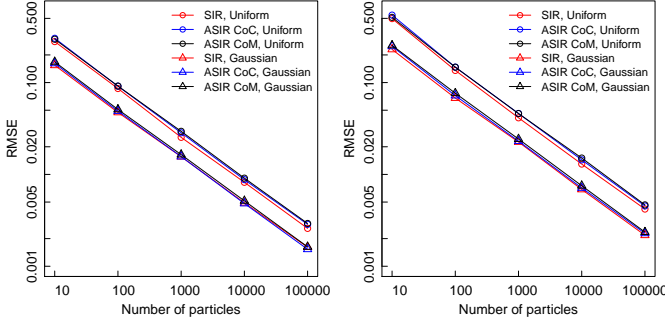


Fig. 6: The “pseudo”-tracking experiment results for the Gaussian prior with $\sigma_{\text{prior}} = 0.5$ and the uniform prior with 3×3 -pixel support (left), and for the Gaussian prior with $\sigma_{\text{prior}} = 0.8$ and the uniform prior with 5×5 -pixel support (right). The state estimation errors of ASIR relative to SIR range between $-12\% \dots +6\%$. The difference between ASIR and SIR decreases as N increases. Both ASIR and SIR converge with increasing number of particles. The RMSE error is reduced by about 30% every time the number of particles doubles, corresponding to a convergence order of \sqrt{N} , as expected for a Monte Carlo method. Error bars are below symbol size.

We performed both theoretical and experimental error analysis of ASIR. We showed that the error in the posterior decreases as the number of particles increases. Moreover, ASIR converges at the same rate as SIR. We presented theoretical upper bounds on the likelihood approximation error as a function of cell size in ASIR. Our analysis was based on the well-known mid-point Riemann-sum approximation of an integral.

We experimentally tested the tracking accuracy and runtime performance of two ASIR variants for image processing: ASIR-1x1 and ASIR-2x2. In our benchmarks, ASIR showed significant speedups over SIR. As more particles are used, the relative speedup over SIR seems to grow exponentially for large-object tracking scenarios, where the likelihood is costly to evaluate. In the presented benchmarks with 12 800 particles, SIR required 5 minutes to track the large object through a 50-frame 2D image sequence. ASIR-1x1 needed only 2.3 seconds to accomplish the same task at the expense of a 2.4% smaller accuracy. ASIR-2x2 completed the task in 5.3 seconds with a 5.8% better tracking accuracy than SIR. This improvement stems from the fact that for some posterior distributions, the piecewise constant likelihood approximate of ASIR may be a more realistic representation of the true posterior than that generated by SIR. This is a known phenomenon [40]. The relative speedups of the two ASIR variants over classical SIR were 130-fold and 57-fold for 12 800 particles, respectively. For larger numbers of particles, we expect even larger speedups.

For small-object tracking, both ASIR variants showed an average 5-fold improvement in execution time for the largest tested particle number. However, the tracking accuracy of ASIR-1x1 is greatly reduced, since the likelihood function has a narrow support that is not well sampled by the coarse bins. While the errors are in the range of 150%, they are

barely visible in the final trajectories since the average RMSE is only about 0.27 pixels. Interestingly, ASIR-2x2 shows improvements both in overall runtime (5-fold) and in tracking accuracy (1%), which suggests that ASIR-2x2 may be a good algorithm for tracking small objects.

We believe that ASIR can be used in many PF applications that require large numbers of particles, costly likelihood evaluations, or real-time performance. When tracking accuracy is not critical, ASIR-1x1 can offer orders of magnitude speedup in image-processing applications. If a loss in tracking accuracy is undesired, ASIR-2x2 still offers significant speedups while in some cases even improving accuracy over SIR. In other applications, one can adjust the size of the averaging bins according to the desired accuracy. Future work will be concerned with further analysis of the effect of bin size on the runtime and the accuracy of ASIR. Further improvements could involve adaptive bin sizes, or higher-order moments of the state distribution within the bin stored on the dummy particle. This outlines an analogy between ASIR and fast multipole methods in particle methods [41].

APPENDIX A PROOF OF THEOREM 1

We analyze the ASIR approximation by mid-point Riemann-sum approximation of an integral. While the dummy particle does not have to be located at the center of a cell, for the sake of simplicity of the derivation, we assume that ASIR uses the mid-point for piecewise constant likelihood approximation. Assume that $f(x, y)$ is twice continuously differentiable in region $D \in \mathbb{R}^{[x_0, x_n] \times [y_0, y_m]}$ and the following partial derivatives are defined: $\frac{\partial^2 f}{\partial x^2} = f_{xx}$, $\frac{\partial^2 f}{\partial y^2} = f_{yy}$ and $\frac{\partial^2 f}{\partial x \partial y} = f_{xy}$. The approximation error $\mathcal{E}_{I_k}(l_x, l_y)$ can be calculated by integrating the multivariate Taylor approximation

$$\begin{aligned} \mathcal{E}_{I_k}(l_x, l_y) &= f(x, y) - f(a, b) \\ &= f_x(a, b)(x - a) + f_y(a, b)(y - b) \\ &\quad + \frac{1}{2!} [f_{xx}(a, b)(x - a)^2 + f_{yy}(a, b)(y - b)^2 \\ &\quad + 2f_{xy}(a, b)(x - a)(y - b)] \end{aligned} \quad (5)$$

over the two-dimensional interval $I_k = [x_{k-1}, x_k] \times [y_{k-1}, y_k]$, where $a = \frac{x_{k-1} + x_k}{2}$, $b = \frac{y_{k-1} + y_k}{2}$, and $D = \bigcup_{k=1}^B I_k$, hence:

$$\begin{aligned} \mathcal{E}_{I_k}(B) &= f_x(a, b) \iint_{I_k} (x - a) dx dy \\ &\quad + f_y(a, b) \iint_{I_k} (y - b) dx dy \\ &\quad + \frac{1}{2!} \left[f_{xx}(a, b) \iint_{I_k} (x - a)^2 dx dy \right. \\ &\quad + f_{yy}(a, b) \iint_{I_k} (y - b)^2 dx dy \\ &\quad \left. + 2f_{xy}(a, b) \iint_{I_k} (x - a)(y - b) dx dy \right]. \end{aligned} \quad (6)$$

Substituting a and b in Eq. (6), we find:

$$\mathcal{E}_{I_k}(l_x, l_y) = \frac{1}{2!} \left[f_{xx}(a, b) \iint_{I_k} \left(x - \frac{x_{k-1} + x_k}{2} \right)^2 dx dy + f_{yy}(a, b) \iint_{I_k} \left(y - \frac{y_{k-1} + y_k}{2} \right)^2 dx dy \right]. \quad (7)$$

We substitute $l_{k_i} = x_k - x_{k-1}$, $l_{k_j} = y_k - y_{k-1}$ and evaluate the integrals. Then Eq. (7) becomes

$$\mathcal{E}_{I_k}(l_x, l_y) = \frac{1}{24} \left[f_{xx}(a, b) l_{k_i}^3 l_{k_j} + f_{yy}(a, b) l_{k_j}^3 l_{k_i} \right]. \quad (8)$$

Next, we sum the absolute values of the partial errors in all I_k regions in order to provide an upper bound on the total approximation error in the closed region $[D]$ as:

$$\mathcal{E}(l_x, l_y) \leq \frac{1}{24} \left[\max_{[D]} |f_{xx}| \max_{k_i} (l_{k_i})^3 \max_{k_j} (l_{k_j}) + \max_{[D]} |f_{yy}| \max_{k_j} (l_{k_j})^3 \max_{k_i} (l_{k_i}) \right]. \quad (9)$$

By substituting l_x and l_y into Eq. (9), we find the total error in the closed region $[D]$:

$$\mathcal{E}(l_x, l_y) \leq \frac{1}{24} \left[\max_{[D]} |f_{xx}| l_x^3 l_y + \max_{[D]} |f_{yy}| l_x l_y^3 \right]. \quad (10)$$

■

APPENDIX B PROOF OF THEOREM 2

For equi-sized square cells, a tighter bound for the approximation error can be derived by repeating the steps that lead to Eq. (8) in Appendix A. The proof diverges here by taking the minimum possible value for the side lengths l_{k_i} and l_{k_j} of the small interval I_k in region $D \in \mathbb{R}^{[x_0, x_n] \times [y_0, y_m]}$, where $D = \bigcup_{k=1}^B I_k$. When I_k is a square with $l = l_{k_i} = x_k - x_{k-1} = l_{k_j} = y_k - y_{k-1}$, we obtain the bound on $\mathcal{E}_{I_k}(l)$ as:

$$\mathcal{E}_{I_k}(l) \leq \frac{l^4}{24} [f_{xx} + f_{yy}]. \quad (11)$$

By summing the absolute values of the errors in all I_k regions, we get the total error in closed region $[D]$:

$$\mathcal{E}(l) \leq \frac{l^4}{24} \left[\max_{[D]} |f_{xx}| + \max_{[D]} |f_{yy}| \right]. \quad (12)$$

■

ACKNOWLEDGMENTS

The authors thank the MOSAIC Group (MPI-CBG, Dresden) for fruitful discussions and the MadMax cluster team (MPI-CBG, Dresden) for operational support. Ömer Demirel was funded by grant #200021–132064 from the Swiss National Science Foundation (SNSF), awarded to I.F.S. Ihor Smal was funded by a VENI grant (#639.021.128) from the Netherlands Organization for Scientific Research (NWO).

REFERENCES

- [1] Arnaud Doucet, Simon Godsill, and Christophe Andrieu. On sequential monte carlo sampling methods for bayesian filtering. *Statistics and computing*, 10(3):197–208, 2000.
- [2] Arnaud Doucet, Nando De Freitas, Neil Gordon, et al. *Sequential Monte Carlo methods in practice*, volume 1. Springer New York, 2001.
- [3] Petar M Djuric, Jayesh H Kotecha, Jianqui Zhang, Yufei Huang, Tadesse Ghirmai, Mónica F Bugallo, and Joaquin Miguez. Particle filtering. *Signal Processing Magazine, IEEE*, 20(5):19–38, 2003.
- [4] Rudolph Emil Kalman et al. A new approach to linear filtering and prediction problems. *Journal of basic Engineering*, 82(1):35–45, 1960.
- [5] Rudolph E Kalman and Richard S Bucy. New results in linear filtering and prediction theory. *Journal of Basic Engineering*, 83(3):95–108, 1961.
- [6] Eric A Wan and Rudolph Van Der Merwe. The unscented kalman filter for nonlinear estimation. In *Adaptive Systems for Signal Processing, Communications, and Control Symposium 2000. AS-SPCC. The IEEE 2000*, pages 153–158. IEEE, 2000.
- [7] Sebastian Thrun, Wolfram Burgard, Dieter Fox, et al. *Probabilistic robotics*, volume 1. MIT press Cambridge, 2005.
- [8] Philip J Davis and Philip Rabinowitz. *Numerical integration*. Blaisdell Publishing Company London, 1967.
- [9] George Brinton Thomas, Ross L Finney, and Maurice D Weir. *Calculus and analytic geometry*, volume 7. Addison-Wesley Reading, Massachusetts, 1984.
- [10] Patric Jensfelt and Steen Kristensen. Active global localization for a mobile robot using multiple hypothesis tracking. *Robotics and Automation, IEEE Transactions on*, 17(5):748–760, 2001.
- [11] Wolfram Burgard, Andreas Derr, Dieter Fox, and Armin B Cremers. Integrating global position estimation and position tracking for mobile robots: the dynamic markov localization approach. In *Intelligent Robots and Systems, 1998. Proceedings., 1998 IEEE/RSJ International Conference on*, volume 2, pages 730–735. IEEE, 1998.
- [12] Wolfram Burgard, Dieter Fox, Daniel Hennig, and Timo Schmidt. Estimating the absolute position of a mobile robot using position probability grids. In *Proceedings of the national conference on artificial intelligence*, pages 896–901, 1996.
- [13] Dieter Fox, Wolfram Burgard, Frank Dellaert, and Sebastian Thrun. Monte carlo localization: Efficient position estimation for mobile robots. *AAAI/IAAI*, 1999:343–349, 1999.
- [14] Sebastian Thrun, Dieter Fox, Wolfram Burgard, and Frank Dellaert. Robust monte carlo localization for mobile robots. *Artificial intelligence*, 128(1):99–141, 2001.
- [15] Sean P Engelson and Drew V McDermott. Error correction in mobile robot map learning. In *Robotics and Automation, 1992. Proceedings., 1992 IEEE International Conference on*, pages 2555–2560. IEEE, 1992.
- [16] Scott Lense and Manuela Veloso. Sensor resetting localization for poorly modelled mobile robots. In *Robotics and Automation, 2000. Proceedings. ICRA'00. IEEE International Conference on*, volume 2, pages 1225–1232. IEEE, 2000.
- [17] J-S Gutmann, Wolfram Burgard, Dieter Fox, and Kurt Konolige. An experimental comparison of localization methods. In *Intelligent Robots and Systems, 1998. Proceedings., 1998 IEEE/RSJ International Conference on*, volume 2, pages 736–743. IEEE, 1998.
- [18] Dieter Fox. Adapting the sample size in particle filters through kld-sampling. *The international journal of robotics research*, 22(12):985–1003, 2003.
- [19] Hatice Köse and HL Akin. The reverse monte carlo localization algorithm. *Robotics and Autonomous Systems*, 55(6):480–489, 2007.
- [20] Yuefeng Wang, Dan Wu, Sepideh Seifzadeh, and Jingxi Chen. A moving grid cell based mcl algorithm for mobile robot localization. In *Robotics and Biomimetics (ROBIO), 2009 IEEE International Conference on*, pages 2445–2450. IEEE, 2009.
- [21] Yuefeng Wang, Dan Wu, and Libing Wu. A dynamic size mcl algorithm for mobile robot localization. In *Robotics and Biomimetics (ROBIO), 2010 IEEE International Conference on*, pages 785–790. IEEE, 2010.
- [22] Fahed Abdallah, Amadou Gning, and Philippe Bonnifait. Box particle filtering for nonlinear state estimation using interval analysis. *Automatica*, 44(3):807–815, 2008.
- [23] Luc Jaulin. *Applied interval analysis: with examples in parameter and state estimation, robust control and robotics*. Springer, 2001.
- [24] Amadou Gning, Branko Ristic, Lyudmila Mihaylova, and Abdallah Fahed. Introduction to box particle filtering. *IEEE Signal Processing Magazine*, pages 1–10, 2012.

- [25] A. Gning, B. Ristic, L. Mihaylova, and F. Abdallah. An introduction to box particle filtering [lecture notes]. *Signal Processing Magazine, IEEE*, 30(4):166–171, 2013.
- [26] John Geweke. Bayesian inference in econometric models using monte carlo integration. *Econometrica: Journal of the Econometric Society*, pages 1317–1339, 1989.
- [27] Anwer S Bashi, Vesselin P Jilkov, X Rong Li, and Huimin Chen. Distributed implementations of particle filters. In *Proc. of the Sixth Int. Conf. of Information Fusion*, pages 1164–1171, 2003.
- [28] Amadou Gning, Lyudmila Mihaylova, and F Abdallah. Mixture of uniform probability density functions for non linear state estimation using interval analysis. In *Information Fusion (FUSION), 2010 13th Conference on*, pages 1–8. IEEE, 2010.
- [29] A. Akhmanova and C. C. Hoogenraad. Microtubule plus-end-tracking proteins: Mechanisms and functions. *Current Opinion in Cell Biology*, 17(1):47–54, 2005.
- [30] Y. Komarova, C. O. de Groot, I. Grigoriev, S. Montenegro Gouveia, E. L. Munteanu, J. M. Schober, S. Honnappa, R. M. Buey, C. C. Hoogenraad, M. Dogterom, G. G. Borisy, M. O. Steinmetz, and A. Akhmanova. Mammalian end binding proteins control persistent microtubule growth. 184(5):691–706, 2009.
- [31] Jo A Helmuth and Ivo F Sbalzarini. Deconvolving active contours for fluorescence microscopy images. In *Advances in Visual Computing*, pages 544–553. Springer, 2009.
- [32] Jo Helmuth, Grégory Paul, and Ivo Sbalzarini. Beyond co-localization: inferring spatial interactions between sub-cellular structures from microscopy images. *BMC bioinformatics*, 11(1):372, 2010.
- [33] I. Smal, E. Meijering, K. Draegestein, N. Galjart, I. Grigoriev, A. Akhmanova, M. E. van Royen, A. B. Houtsmuller, and W. Niessen. Multiple object tracking in molecular bioimaging by Rao-Blackwellized marginal particle filtering. 12(6):764–777, 2008.
- [34] William J Godinez, Marko Lampe, Peter Koch, Roland Eils, Barbara Muller, and Karl Rohr. Identifying virus-cell fusion in two-channel fluorescence microscopy image sequences based on a layered probabilistic approach. *Medical Imaging, IEEE Transactions on*, 31(9):1786–1808, 2012.
- [35] I. Smal, K. Draegestein, N. Galjart, W. Niessen, and E. Meijering. Particle filtering for multiple object tracking in dynamic fluorescence microscopy images: Application to microtubule growth analysis. 27(6):789–804, 2008.
- [36] D. Thomann, D. R. Rines, P. K. Sorger, and G. Danuser. Automatic fluorescent tag detection in 3D with super-resolution: Application to the analysis of chromosome movement. 208(1):49–64, 2002.
- [37] Bo Zhang, Josiane Zerubia, and Jean-Christophe Olivo-Marin. Gaussian approximations of fluorescence microscope point-spread function models. *Applied Optics*, 46(10):1819–1829, 2007.
- [38] Michael K Cheezum, William F Walker, and William H Guilford. Quantitative comparison of algorithms for tracking single fluorescent particles. *Biophysical journal*, 81(4):2378–2388, 2001.
- [39] Ömer Demirel, Ihor Smal, Wiro Niessen, Erik Meijering, and Ivo F. Sbalzarini. Ppf - a parallel particle filtering library. *arXiv preprint arXiv:1310.5045*, 2013.
- [40] Eugenia Koblents and Joaquin Miguez. A population monte carlo scheme for computational inference in high dimensional spaces. In *ICASSP*, 2013.
- [41] Leslie Greengard and Vladimir Rokhlin. A fast algorithm for particle simulations. *Journal of computational physics*, 73(2):325–348, 1987.